Enabling Photoemission Electron Microscopy in Liquids via Graphene-Capped Microchannel Arrays

Hongxuan Guo,[1,2] Evgheni Strelcov,[1,2] Alexander Yulaev,[1,2,3] Jian Wang,[4] Narayana Appathurai,[4]

Stephen Urquhart,[5] John Vinson,[6] Subin Sahu,[1,2,7] Michael Zwolak,[1] and Andrei Kolmakov[1*]

* Corresponding author: andrei.kolmakov@nist.gov.

[1]Center for Nanoscale Science and Technology, NIST, Gaithersburg, MD 20899
[2]Maryland NanoCenter, University of Maryland, College Park, MD 20742
[3]Department of Materials Science and Engineering, University of Maryland, College Park, MD 20742, USA
[4]Canadian Light Source, Saskatoon, SK S7N 2V3, Canada
[5]Department of Chemistry, University of Saskatchewan, Saskatoon, SK S7N 5C9, Canada
[6]Material Measurement Laboratory, NIST, Gaithersburg, MD 20899, USA
[7]Department of Physics, Oregon State University, Corvallis, OR 97331, USA

Supporting Information

Molecular dynamics simulations of water near graphene and a comparison with the Au interface.
Figure S1a shows the full simulation cell for water in a graphene-capped channel. The simulation cell consists of two parallel double-layer sheets of single layer graphene of cross- section 1.2 nm by 1.2 nm with 2 nm of vacuum in between them, as shown in Fig. S1a, and with 100 water molecules initially placed on the opposite sides of each layer. Since periodic boundary conditions are used in all directions, this configuration is the equivalent of having 200 water molecules between two double layers of graphene. The position of the carbon atoms and cross-section of the box are kept fixed during the equilibration and production run.
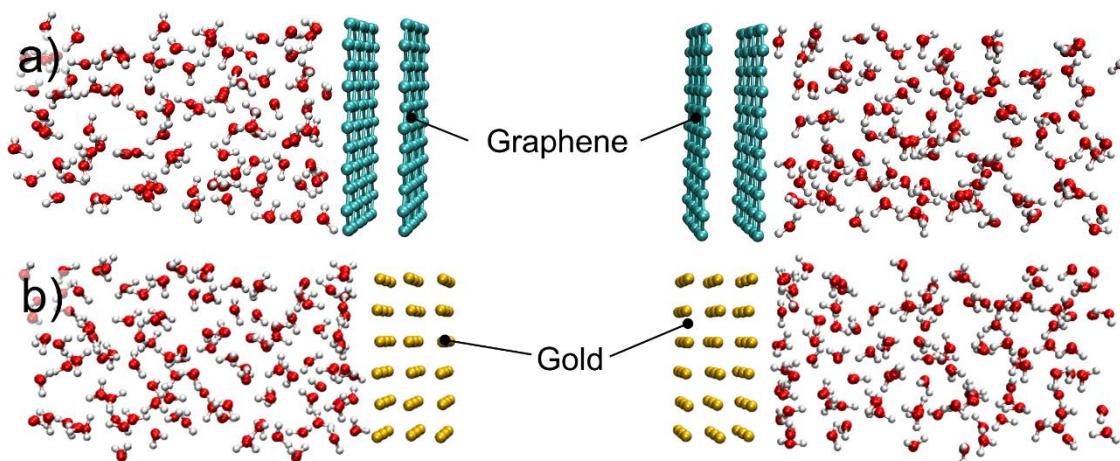

Figure S1. A snapshot from the MD simulation of water channel capped with **a** graphene and **b** gold. This is the full unit cell and the simulation is periodic in all directions. Carbon and gold atoms are frozen during the simulation and, since there is periodicity in all directions, the water molecules can move around the boundary. The cross-section of the cell is kept fixed during an entire simulation but the height of the box was adjusted during equilibration to obtain the targeted pressure and temperature.

We also perform MD simulations for gold-capped, water channels, see Fig.S1b. Here, the simulation cell consists of two sheets of gold each of cross-section 1.24 nm by 1.24 nm separated by 1.58 nm of vacuum on one side and 291 water molecules on the other. Each sheet has three layers of gold atoms that are frozen during the simulation, where we use the (100) surface of the face-centered cubic (fcc) structure. The parameters for the van der Waals interaction between gold and water are from the Ref. 1. The remaining simulation details are the same as the graphene-capped water channel. Our model does not take into account polarization of the metal due to interaction with water. Individual water molecules can produce a significant image potential on gold. For large numbers of water molecules, however, this image potential becomes insignificant due to the averaging out of dipole orientations[2]. Other studies show that polarization does not have a significant effect on interfacial water structure[3]. Since the dominant effect in gold is the screening of the core hole, any small structural change due to polarization or other interactions will not substantially change the XAS spectrum.

For determining whether two water molecules are hydrogen bonded, we use the criteria that the oxygen-oxygen distance is less than 0.35 nm and the oxygen-oxygen-hydrogen angle is less than 35° (see Ref. 4). The molecules are counted as double donor (DD), single donor (SD), and non-donor (ND) when the number of hydrogen atoms contributing to hydrogen bonds is two, one, and zero, respectively (Figure S2).
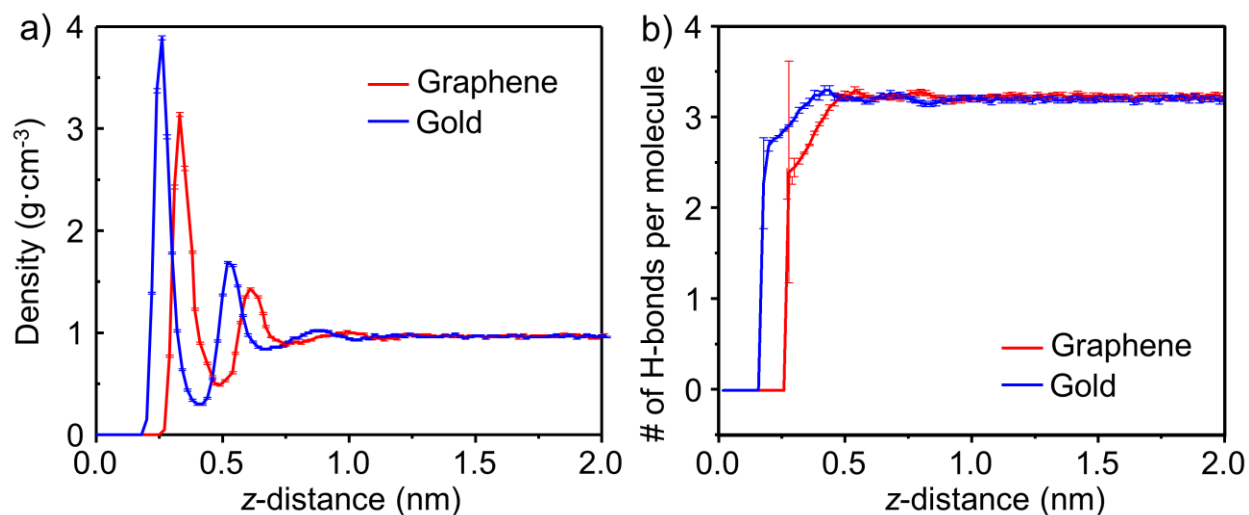

Figure S2. **a,** Density profile for water adsorbed on graphene and gold as a function of distance from the interface. In both cases, oscillations are induced by the presence of the surface, with gold giving rise to slightly stronger oscillations than graphene; **b,** Hydrogen bonds per water molecule vs. distance, z, from the

graphene/gold surface. The number of hydrogen bonds rapidly approaches the bulk value away from the surface. Nearby the surface, however, the number of hydrogen bonds is depleted by about 25 %.

Oxygen K-edge XAS Calculations

The OCEAN code requires the one-electron wavefunctions of the ground-state system as an input for the Bethe-Salpeter equation (BSE). For this we use density functional theory (DFT) within the local density approximation as parameterized by Ceperley, Alder, Perdew, and Wang[5]. We make use of the QuantumESPRESSO code[6], and take advantage of an efficient k-point interpolation scheme[7]. The BSE approach retains two electron-hole interaction terms in addition to the non-interacting DFT Hamiltonian; the attractive direct and repulsive exchange. We calculate these explicitly using a combination of a local and a real-space basis. A pseudopotential inversion scheme is necessary to reconstruct the all-electron character of the DFT conduction-band states near the core hole[5]. Within the BSE, the dielectric response of the system screens the direct interaction, for which we take the random phase approximation coupled with a model dielectric function to capture the long-range response[8].
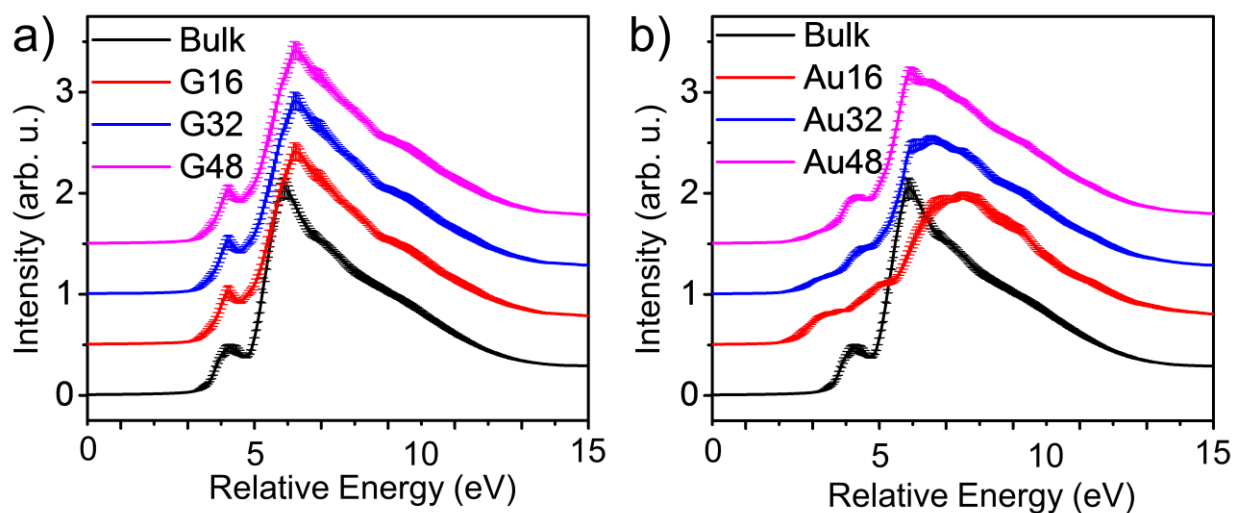

Figure S3. The changes in the XAS water spectra with averaging over the first 16, 32, or 48 water molecules for both **a** water interfacing graphene and **b** water interfacing gold. While both become more bulk-like as further water molecules are included, the changes in the spectrum of the gold-interfacing water are much more dramatic. Spectra are *y*-offset for clarity of presentation.

We use an energy cut-off of 952 eV (70 Ryd.) for the DFT calculations and calculate DFT states at the Gamma point. The k-point interpolation scheme expands this to a 2 × 2 × 2 k-point mesh for the x-ray calculations. For the graphene surface we use a 1.2 nm by 1.2 nm by 4.0 nm box containing 128 water molecules and 132 carbon atoms. For the gold this was changed to a 1.224 nm by 1.224 nm cross

section with 36 gold atoms. The screening calculation uses 9000 bands, covering a range of 100 eV above the Fermi level. The BSE states include 5100 bands of which approximately 4456 (4390) were unoccupied for the graphene (gold) surface cells – with a metallic surface layer not all k-points will have the same number of occupied bands. The local basis for calculating the exchange and short-range components of the direct interaction consists of four projectors per angular momentum channel for s-d and three for f. The real-space basis is a regular 24 × 24 × 80 grid. The bulk cells contain 226 water molecules within a 1.8 nm by 1.8 nm by 2.1287 nm box and the real-space basis is a 32 × 32 × 40 grid. All other parameters are the same as for the cells with surfaces. The long-range part of the dielectric response to the core-hole potential is calculated using a model dielectric function. For all three setups, we used the bulk water dielectric constant of 1.8.

The reduced strength of the post-edge feature in the O K edge of water is commonly observed in both the BSE calculations used here[9] and the delta-SCF approach used in other work[10]. This is due to the fact that the pre-edge and main-edge features (originating from 4a1 and 2b2 of isolated molecule) are localized and therefore their relative intensities are highly sensitive to details of the potential. The latter one depends sensitively on inaccuracies in screening of the core-hole potential.

Despite this, changes in the calculated spectra in response to changes in structure, from bulk water to water on a surface, can be meaningfully compared to changes measured in experiment. In Fig 2c we show that, despite the structural changes due to the graphene bi-layer, the O K-edge XAS changes only slightly compared to that of bulk water.

Details of the BLU analysis

As mentioned in the main text, the number of spectral components for BLU analysis must be provided by the researcher and can be estimated using principal component analysis (PCA) or by under- and oversampling. Figure S4 presents a case of oversampling: unmixing the PEEM spectral dataset of Figure 3 (main text) into 6 components. As can be seen, the two new component arise due to the splitting of C2 and C4 into two parts. The new component C2' (Fig. S4 b&h) is very similar to the old C2 both in its abundance map and its spectrum. The C2'' component (Fig. S4 c&i), though, is different, and clearly unnecessary. Its average abundance across the map is only about 30 %, and its contribution to the overall picture is higher than 70 % in only a few pixels. The endmember of the C2'' component (Fig. S4i) has slanted shape with several tiny carbon and oxygen peaks. Overall, this component does not add to the understanding of the sample's behavior and should not be separated from C2'.

The C4'-C4'' pair, on the other hand, presents a much more physically meaningful picture despite oversampling. These components highlight the core and peripheral sites of two water-filled channels with prominent radiolysis. The difference between their spectra (Fig. S4 k&l) is perfectly clear in the light of the main text explanations of the water redistribution and bubble formation processes. The core of the cell is affected by bubble formation earlier than the periphery, and therefore the spectrum of the peripheral component C4'' (Fig. S4l) is closer to the normal water spectrum (Fig. S4j), than that of the core component C4' (Fig. S4k). The C4' spectrum plummets at 536.5 eV, whereas the C4'' intensity drops later, at 337.7 eV. Since the bubble radial expansion is a gradual process, and BLU considers data at every pixel as a linear combination of position-independent components, the total number of independent components correctly describing a behavior of dynamic water channels should be equal to the number of pixels in the cell radius. Yet, as shown in the main text, their behavior can be understood by unmixing the dataset into only four components.
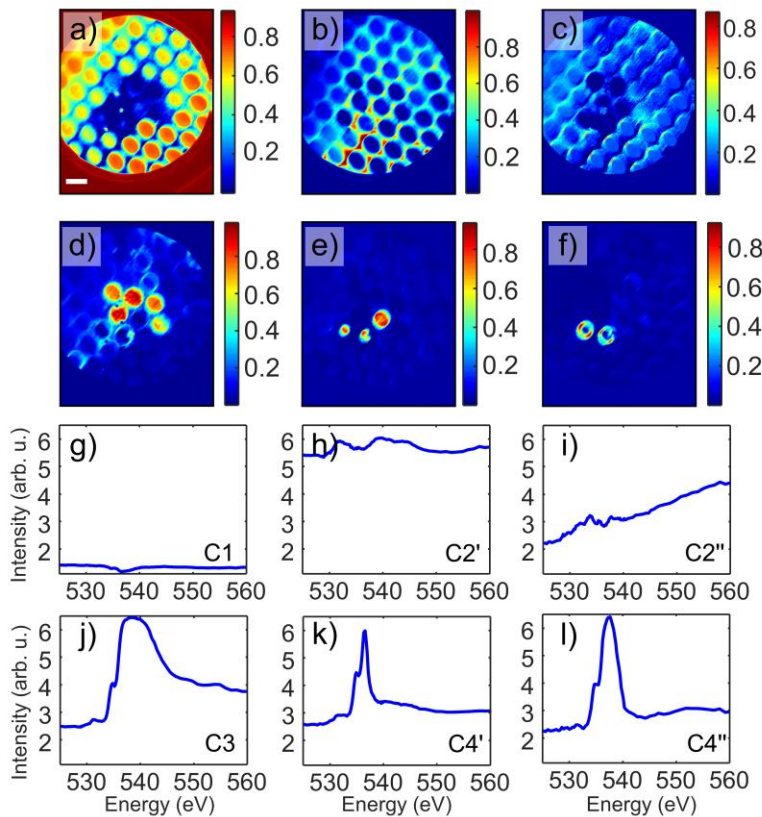

Figure S4. BLU of a PEEM spectroscopic dataset into 6 components: C1 - panels **a** & **g** empty channels and aperture; C2' - panels **b** & **h** MCA walls; C2'' - panels **c** & **i** weaker signal of MCA walls & contaminants; C3 - panels **d** & **j** water-filled static channels; C4' - panels **e** & **k** water-filled dynamic channels cores; and C4'' - panels **f** & **l** water-filled dynamic channels periphery. Abundance maps (component intensity as a fraction of unity) and

corresponding endmember spectra are shown. The scale bar is 10 µm. Spectra are displayed on the same scale for comparison.

An improvement of unmixing for two cells highlighted by C4'' component can also be seen by comparing the BLU error maps for 4 and 6 components (Fig. S5 a&b, respectively). The core region of one of these cells, when unmixed into 4 components, had an error of about 9 %, and after 6-component unmixing the error dropped down to about 5 %. However, in both cases error for most of the sample is well below 10 %, showing once again that 4-component unmixing is sufficient.
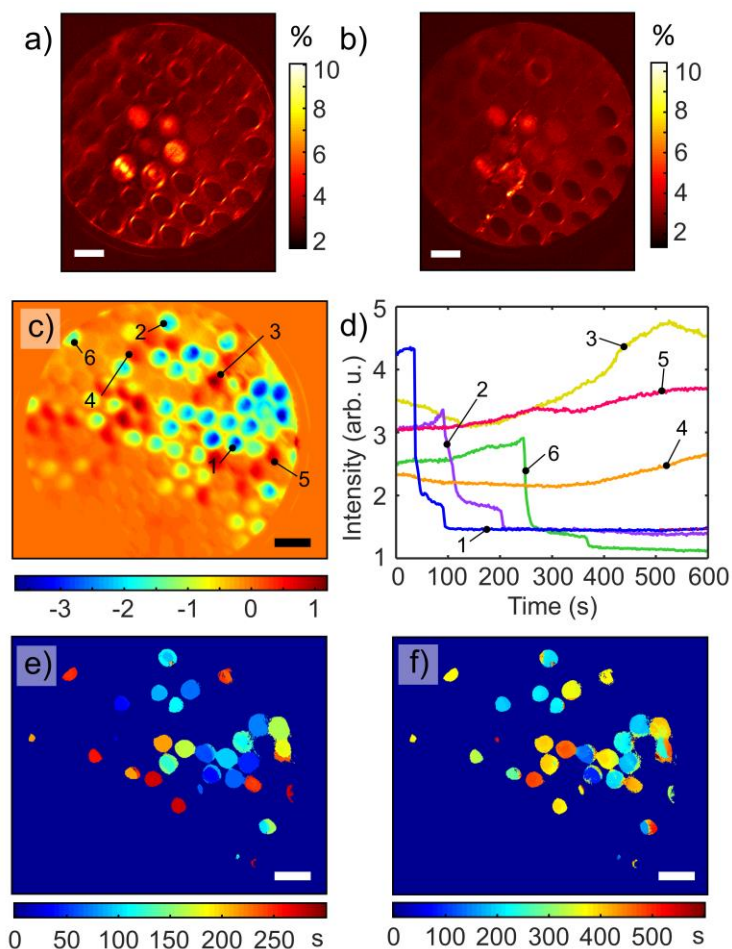

Figure S5. PEEM data analysis: **a** & **b**, BLU Error maps for 4 and 6 components, respectively; **c**, the map of the difference between the initial and final XAS intensity of the temporal PEEM dataset of Figure 3 (main text); **d**, Intensity vs. time curves averaged over the central regions (500 nm × 500 nm) of channels indicated in panel **c** and displaying representative behaviors; **e** & **f**, maps of the times at which the first and last drops in the XAS intensity occurred (correspond to steps seen in curves 1, 2 &6 of panel **d**. The scale bars in all images are 10 µm.

To highlight the difference between the 3 groups of cells classified in the main text for the temporal PEEM dataset, Figure S5c presents the difference between the initial and final XAS intensity across the sample. This procedure helps immediately identify empty cells (no changes, orange color), cells with

increasing intensity (red color) and cells where the signal drops (blue color). For comparison, Figure S5d also presents XAS intensity vs. time plots from several cells in panel c. Note that although the curve of cell 6 has steps similar to those of cells 1 and 2, its final intensity is much lower. This is a consequence of the cell 6 spatial position in the region of the sample where excitation irradiation is lower than in the central regions, where cells 1 and 2 are located. When normalized to the local irradiation intensity, the curves look similar and their final intensity values are very close.

Figures S5e and f also present spatial maps of times at which the first and last step-like drops in intensity occurred. Despite the individual cells proximity to each other, they appear to behave independent of one another, which suggests that they do not exchange liquid through the frontal or backside MCA surface leakage.

In principle, the oxidation of the graphene membrane with radiolysis products (H_2O_2, $OH^\cdot$, $O^\cdot$) may result in the loss of membrane integrity and water evaporation into the ambient vacuum. Such events can be discriminated from the bubble formation cases by their lowest TEY intensity from the disrupted channels.

The formation of the "wetting layer" and supporting SEM studies

Attenuation estimations

The ratio between the signal intensity produced by n monolayers of water to the intensity produced by bulk water is given by:

$$\frac{I_w^n}{I_w^\infty} = 1 - e^{-\frac{h}{\lambda_w}}$$

, (1)

where h is the thickness of n water monolayers, and λ_w is the inelastic mean free path of electrons in liquid water. Experimental intensities can be written as: $I_0 = I_w^\infty \cdot \alpha + I_g$ and $I_1 = I_w^n \cdot \alpha + I_g$, where α is the attenuation coefficient associated with the graphene membrane, and $I_g = I_2$ is the signal originating in the graphene. Thus, the number of water layers corresponding to the I_1 step is:

$$N = -\frac{\lambda_w}{a} \cdot ln\left(1 - \frac{I_1 - I_2}{I_0 - I_2}\right)$$

, (2)

where a = 0.25 nm was used as an effective thickness of a water monolayer. The numerical value of N depends on the electron inelastic mean free path in water which has not been unequivocally determined yet. [11,12] Assuming Auger electrons ($E_k \approx 500$ eV)[13] to be the fastest and dominant fraction in

the TEY signal having the largest inelastic mean free path, Figure 3f presents a map of the number of the I_1-step water layers calculated taking λ_w = 2.5 nm.

SEM experiments

Similar to x-rays, liquid water in the sealed micro-channel may undergo a radiolysis, with the formation of bubbles, evaporation, re-condensation and extensive diffusion upon electron beam irradiation. Figures S6a and S6b demonstrate SEM snapshots taken two seconds apart with several empty channels, one of which is covered with graphene membrane, and a water-filled channel at the center. The SEM signal intensity across the images can be classified into several regions having characteristic gray scale regions: brightest MCA surface (1), darkest MCA channels with no graphene (2), regions with strong water signal (3), pristine graphene membrane (4) and regions with weak water signal (5). Notice that the pristine graphene membrane signal (4) has the same value both in the open empty channel and the water-filled channel (Fig.S6 b). The water distribution within the central channel is very dynamic upon electron beam irradiation, drastically changing over 2 seconds: patches of dry graphene not only significantly grow in size, but also change shapes, merging into one large domain. The circular geometry of the channel allowed us to introduce polar coordinates as shown in Figure S6a, to average SEM signal over the polar angle and present it in the form of a 2D time-r-distance diagram in Figure S6c. This diagram, as well as its sections shown in Figure S6d, clearly demonstrate the same „quantized" behavior of the water signal very similar to that we observed in the time-resolved PEEM data. Between the SEM signal levels of the MPC walls (largest) and graphene (lowest), there are two spatially separate and distinct levels of gray scale value, labeled as a "thick water" and a "thin water", that presumably correspond to bulk water and one monolayer of water, respectively. Their spatial distribution is also quite similar to that observed in the PEEM data, the "thick water" towards the periphery and "thin water" covering the center part of graphene. The presented SEM images also imply the possible existence of sub-monolayer water layers (in Fig. 3f (main text) cores of some channels contain 0.5 to 0.8 monolayers): an apparent sub-monolayer is a spatial mix of dry graphene regions and monolayer-covered patches that PEEM cannot resolve spatially.
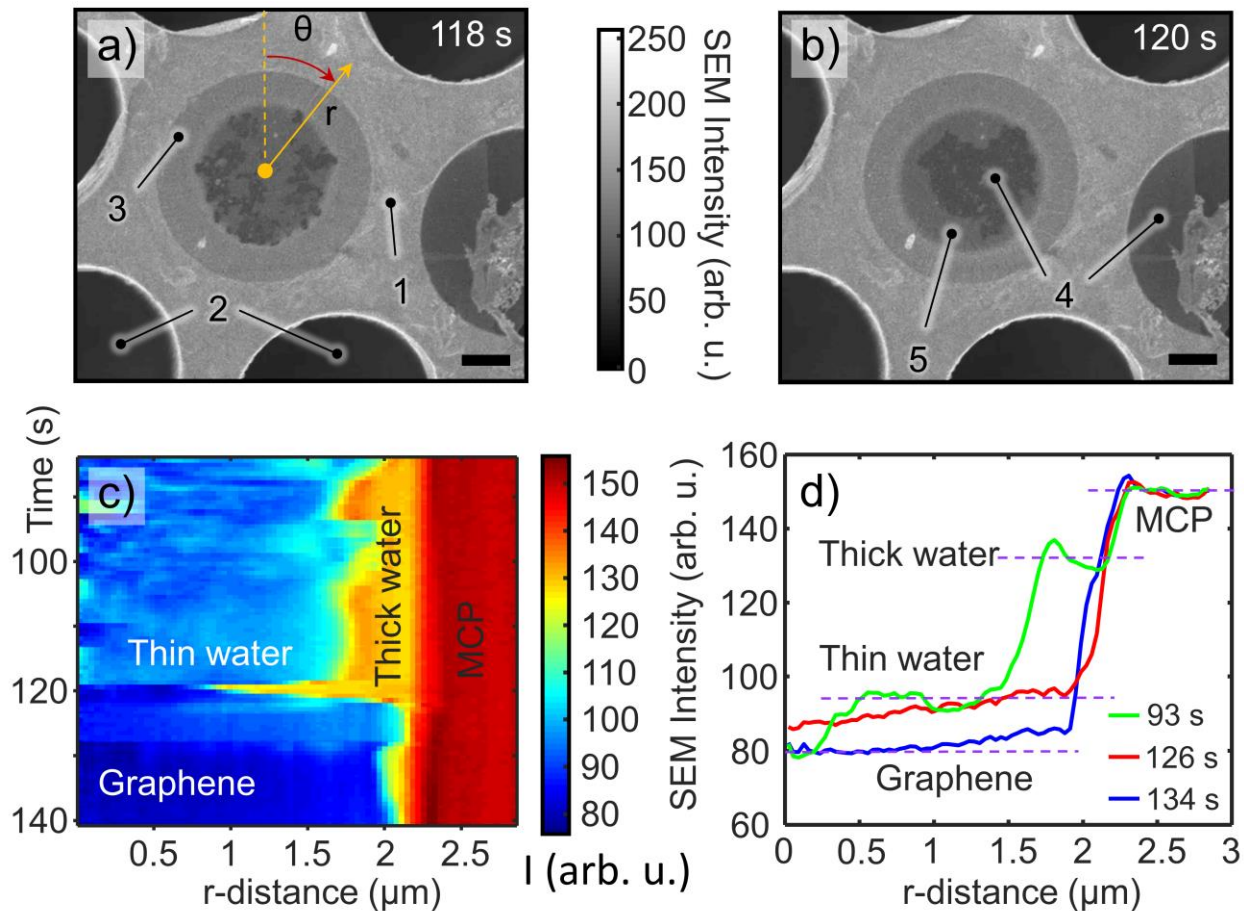
Figure S6. SEM imaging of MCA-G devices: **a** and **b,** images of an MCA-G region with a water-filled channel (center), several empty channels, and an empty channel with a suspended graphene membrane (right part of images) as captured 2 seconds apart during the water redistribution process (images taken from the video in SI). The signal intensity on the MCA wall (1) is 140 to 150 units, in empty channels (2) is 40 to 50 units, the thick water layer in the filled channel (3) is 120 to 130 units, the thin water layer in the filled channel (5) is 98 to 103 units, and on the empty graphene membrane (4) is 80 to 85 units; **c,** SEM intensity averaged over the full circle (angle θ in a) and plotted as a function of radius-vector (r in a) distance and time; **d,** Selected radial profiles from panel **c** for three different times showing signal strength for the MCA wall, graphene and two discrete water thicknesses formed during the redistribution process. The scale bars in **a** and **b** are 10 μm.

The channels topography

The topography of the graphene capped channels depends on a few factors: the media behind the channel (empty, liquid, bubble) and residence time in vacuum. Figure S7 shows the shape of graphene membrane in a water-filled, empty, and bubble containing channels as measured in AFM tapping (AC) mode under vacuum conditions. Both topographic images and their cross-sections (Fig. S7 bottom raw) imply that graphene is sufficiently strongly adhered to the liquid surface in the filled cell and takes a concave shape with a typical stretch between 200 nm and 500 nm for this diameter of the channel. In the empty channel the graphene membrane is flat, recessed ca. 150 nm lower than the MCA top plane.

The concave shape of the capped filled channel is a result of the leakage induced pressure drop inside the channel from atmospheric (just after the channel sealing) to saturated vapor pressure (ca. 2 kPa) when in vacuum.
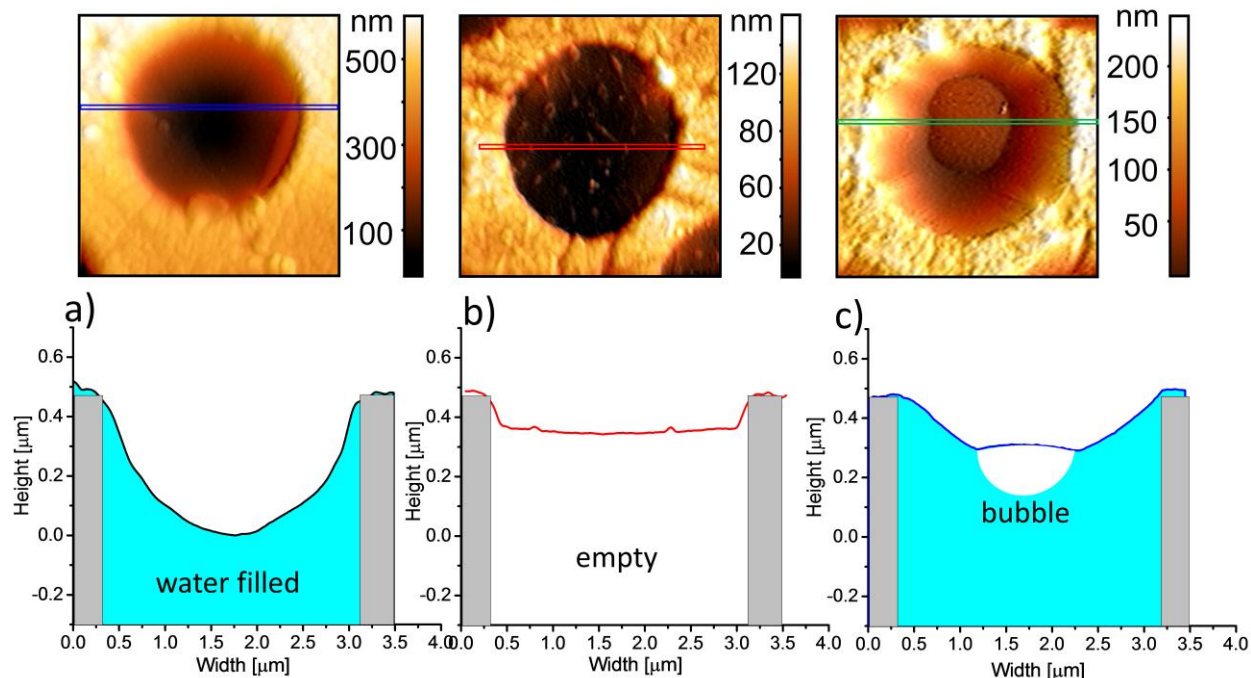

Figure S7. AFM topographic images of MCA-G devices in vacuum: a water-filled channel **a**, an empty channel with suspended graphene membrane **b**; a filled channel with bubble formed under graphene **c**; The bottom row depicts the corresponding topographic profiles measured along the selected lines (top raw). Note that *Height* and *Width* axes are not on the same scale.

The detailed mechanisms of bubble formation under hydrophobic graphene is a subject of the ongoing research. Based on our SEM and PEEM observations, the bubble formation in MCA platform is strongly radiation dose dependent implying that radiolysis is a major mechanism. Briefly, when X-ray photons with the energies of 540 eV (O *K*- absorption edge) irradiate water inside the channel under the grazing angle, a high density of radicals is created within very thin (*L* ≈500 nm, soft X-ray 540 eV attenuation length) water layer. The multiple reaction and recombination paths result in primary accumulation of molecular hydrogen in this layer.[14] Under conditions when the recombination reactions and runaway diffusion of hydrogen are slower compared to its generation rate, concertation of hydrogen under the graphene grows until the saturation concertation of hydrogen in water is achieved. The latter depends on the pressure inside the channel. Oversaturation above this concertation causes stochastic formation of a microbubble.

X-rays induced bubble formation thresholds

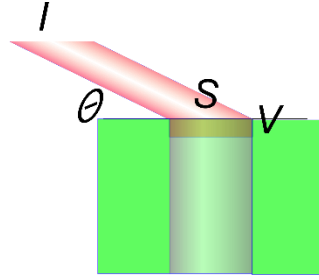Here we estimate photon flux which is required to form hydrogen bubble at maximum of X-rays absorption.

Figure S8. The geometry of the X-ray irradiation of the MCA channel with photon flux *I*. Here *S*, *V* and *θ* stand for channel area, excitation volume and irradiation angle correspondingly

We denote the X-rays radiation power as $P = E_{pho}I$, where, E_{pho} is the energy of the X-ray photon (540 eV), and I is the photon flux $[\mathrm{s^{-1}cm^{-2}}]$. S is the cross section area of the microchannel and V is the irradiated water volume (excitation volume). For the used PEEM setup, the angle between the SR beam and the surface of the graphene is $\theta = 16°$. Then, the volumetric dose rate for V is

$$\Psi = \frac{P \cdot S \cdot \sin(\theta)}{\rho \cdot S \cdot d} = \frac{E_{pho} \cdot I \cdot S \cdot \sin(\theta)}{\rho \cdot S \cdot L \cdot \sin(\theta)} = E_{pho}I / (L\rho)$$

Where, L is X-rays attenuation length ≈0.5 um for 540 eV photon energy,[15] and ρ is the density of water. One can estimate the volumetric molecular hydrogen production rate R using the approach developed in[14]

$$R_{H_2} = \rho \Psi \frac{G(H_2)}{eN_A}$$, here G is G-factor for hydrogen $G(H_2)$ = 0.44 molecules/100 eV

With irradiation, the concentration of the H_2 in the water increases until reverse recombination reactions together with diffusional runaway equilibrate the process. The steady state concentration correlates with the volumetric dose-rate as a power law: [16]

$$C_{steady-H_2} = A_{H_2} \Psi^{\gamma_{H_2}} = A_{H_2} (E_{pho}I / (L\rho))^{\gamma_{H_2}}$$

Then, the corresponding photon flux can be estimated as

$$I = \frac{L\rho}{E_{pho}} (\frac{C_{steady-H_2}}{A_{H_2}})^{\frac{1}{\gamma_{H_2}}}$$

The onset of a bubble formation via homogeneous nucleation requires very large supersaturation over $C_{\text{steady}-H_2}$ and experimentally measured value is $C_{\text{homog}-H_2} \sim 190 \, \text{mmol}/L$.[17] On the other hand, heterogeneous nucleation of H_2 at water-graphene interface may occur at any value below $C_{\text{homog}-H_2}$ as soon as $C_{\text{steady}-H_2}$ exceeds the saturation concertation C_{sat} of molecular hydrogen in water. [17]

The latter, however, depends on the pressure inside the channel via Henry's Law for H_2 in water. We do not know the pressure inside the channel exactly but for evaluation purposes can use two ultimate values: saturated water vapor pressure (2 kPa) or atmospheric pressure (100 kPa).

Then, assuming C_{sat}(2 kPa) ~ 2.1x 10^{-5} mol/L , and C_{sat}(100 kPa) ~ 0.8x 10^{-3} mol/L

$A_{H_2} \sim 9.3 \times 10^{-7} \, \text{mol}/L \, (\text{s/Gy})^{-\gamma_{H_2}}$, $\gamma_{H_2} \sim 0.44$ for water at PH 6[16] one can get:

$I_{(2\text{kPa})} \approx 7 \times 10^{11} \text{s}^{-1} \text{cm}^{-2}$, $I_{(100\text{kPa})} \approx 3 \times 10^{15} \text{s}^{-1} \text{cm}^{-2}$ This two numbers have to be compared to the photon flux in our experiment: $I_{\text{exp}} \approx 10^{15} \div 10^{16} \text{s}^{-1} \text{cm}^{-2}$ (depending on alignment) and to the flux required for homogenous bubble nucleation:

$I_{\text{homog}} \approx 8 \times 10^{20} \text{s}^{-1} \text{cm}^{-2}$.

As can be seen, the radiolytic hydrogen bubbles can indeed be created under our experimental conditions, and the presence of the graphene interface facilitates this process. To reduce the radiolytic effects few procedures can be undertaken:

a) The channel's design has to be fluidic thus the radiolysis products can be rapidly removed from the excitation volume

b) The pressure inside the cell can be elevated to increase C_{sat}

c) Working with harder X-rays with lower photo-absorption cross section.

References

1.   Schravendijk, P.; van der Vegt, N.; Delle Site, L.; Kremer, K., Dual-Scale Modeling of Benzene Adsorption onto Ni (111) and Au (111) Surfaces in Explicit Water. *ChemPhysChem* **2005,** *6* (9), 1866-1871.
2.   Shelley, J.; Patey, G.; Bérard, D.; Torrie, G., Modeling and structure of mercury-water interfaces. *The Journal of chemical physics* **1997,** *107* (6), 2122-2141.
3.   Kohlmeyer, A.; Witschel, W.; Spohr, E., Molecular dynamics simulations of water/metal and water/vacuum interfaces with a polarizable water model. *Chemical physics* **1996,** *213* (1), 211-216.

4.   Luzar, A., Resolving the hydrogen bond dynamics conundrum. *The Journal of Chemical Physics* **2000,** *113* (23), 10663-10675.

5.   Perdew, J. P.; Wang, Y., Pair-distribution function and its coupling-constant average for the spin-polarized electron gas. *Physical Review B* **1992,** *46* (20), 12947.

6.   Giannozzi, P.; Baroni, S.; Bonini, N.; Calandra, M.; Car, R.; Cavazzoni, C.; Ceresoli, D.; Chiarotti, G. L.; Cococcioni, M.; Dabo, I., QUANTUM ESPRESSO: a modular and open-source software project for quantum simulations of materials. *Journal of physics: Condensed matter* **2009,** *21* (39), 395502.

7.   (a) Prendergast, D.; Louie, S. G., Bloch-state-based interpolation: An efficient generalization of the Shirley approach to interpolating electronic structure. *Physical Review B* **2009,** *80* (23), 235126; (b) Shirley, E. L., Optimal basis sets for detailed Brillouin-zone integrations. *Physical Review B* **1996,** *54* (23), 16464.

8.   Shirley, E. L., Local screening of a core hole: A real-space approach applied to hafnium oxide. *Ultramicroscopy* **2006,** *106* (11), 986-993.

9.   Vinson, J.; Kas, J. J.; Vila, F. D.; Rehr, J. J.; Shirley, E. L., Theoretical optical and x-ray spectra of liquid and solid H_2O. *Physical Review B* **2012,** *85* (4), 045101.

10.   (a) Velasco-Velez, J.-J.; Wu, C. H.; Pascal, T. A.; Wan, L. F.; Guo, J.; Prendergast, D.; Salmeron, M., The structure of interfacial water on gold electrodes studied by x-ray absorption spectroscopy. *Science* **2014**; (b) Prendergast, D.; Galli, G., X-Ray Absorption Spectra of Water from First Principles Calculations. *Phys. Rev. Lett.* **2006,** *96* (21), 215502.

11.   Nikjoo, H.; Uehara, S.; Emfietzoglou, D.; Brahme, A., Heavy charged particles in radiation biology and biophysics. *New Journal of Physics* **2008,** *10* (7), 075006.

12.   Ottosson, N.; Faubel, M.; Bradforth, S. E.; Jungwirth, P.; Winter, B., Photoelectron spectroscopy of liquid water and aqueous solution: Electron effective attenuation lengths and emission-angle anisotropy. *Journal of Electron Spectroscopy and Related Phenomena* **2010,** *177* (2–3), 60-70.

13.   Slavíček, P.; Kryzhevoi, N. V.; Aziz, E. F.; Winter, B., Relaxation Processes in Aqueous Systems upon X-ray Ionization: Entanglement of Electronic and Nuclear Dynamics. *The Journal of Physical Chemistry Letters* **2016,** *7* (2), 234-243.

14.   Grogan, J. M.; Schneider, N. M.; Ross, F. M.; Bau, H. H., Bubble and Pattern Formation in Liquid Induced by an Electron Beam. *Nano Letters* **2014,** *14* (1), 359-364.

15.   Technology, N. I. o. S. a., X-Ray Form Factor, Attenuation and Scattering Tables (version 2.1). Chantler, C.T., Olsen, K., Dragoset, R.A., Chang, J., Kishore, A.R., Kotochigova, S.A., and Zucker, D.S. : Gaithersburg, MD., 2005.

16.   Joseph, J. M.; Seon Choi, B.; Yakabuskie, P.; Clara Wren, J., A Combined Experimental and Model Analysis on the Effect of pH and O2(aq) on Γ-radiolytically Produced H_2 and H_2O_2. *Radiat. Phys. Chem.* **2008,** *77*.

17.   Finkelstein, Y.; Tamir, A., Formation of Gas Bubbles in Supersaturated Solutions of Gases in Water. *AIChE journal* **1985,** *31*, 1409.